AD-A090 644 ROCKWELL INTERNATIONAL SEAL BEACH CA F/G 9/4
BACKGROUND MOTION EFFECTS ON STARING SENSORS AND THE RELATIVE E--ETC(U)
1980 A K MUKHOPADHYAY, W H HAAS

UNCLASSIFIED NL

1 of 1
AD A090644

END
DATE FILMED
11-80
DTIC

BACKGROUND MOTION EFFECTS ON STARING SENSORS AND THE RELATIVE EFFECTIVENESS OF SIGNAL PROCESSING FILTERS IN MINIMIZING SUCH EFFECTS ON TARGET DETECTION

A.K. Mukhopadhyay W.H. Haas
Members of Technical Staff, Rockwell International Corp.
Seal Beach, CA

Abstract

The objectives of this study are to characterize apparent background motion as a function of observer-satellite orbit and sighting geometry and then to compare the effectiveness of signal processing filters in minimizing background motion effects on target detection. For many applications, complex algorithms cannot be realized economically, so simple yet effective algorithms must be developed to do the job. In this study both ideal and optimum third-order temporal recursive filters were synthesized and their simulated signal-to-noise ratio performance compared with that obtained by simple temporal differencing (first- through fourth-order). Our results indicate that for the same amount of memory, compared to the differencing filters, significant SNR performance improvement can be achieved with optimum recursive filters at the cost of a modest increase in filter complexity. The study is particularly pertinent to the detection by a staring mosaic sensor of aircraft from satellites in high (> 1000 km) orbits. They are typically dim targets flying close to a structured background (the earth surface), and the background clutter tends to dominate the detection problem.

I. Introduction

Staring mosaic sensors are effective in minimizing possible "noise" from background spatial structure by taking differences between successive frames of data and thereby eliminating features which have spatial but not temporal variation. This is commonly referred to as background subtraction. Thus in space surveillance, the star background can be eliminated by an inertially stabilized staring sensor while "targets" (satellites which move through the field of view) are detected as streaks. Detection of objects against an earth background is more difficult because the staring feature cannot be ideally achieved. In any orbit except synchronous equatorial, an earth-looking sensor can effect perfect staring at only one point in the FOV because of both satellite motion and earth motion. All other background points in the FOV will appear to drift, and this motion causes "noise" signals if the background has appreciable spatial structure to simulate one or more temporally moving targets. Even in a synchronous equatorial orbit, attitude drift of the sensor is of concern in establishing ideal staring operation. The "expansion" and "contraction" of the FOV, depending on the satellite zenith angle, is shown in Fig. 1 (earth curvature over the satellite FOV is ignored).

A critical problem in the design of signal processing systems for large staring mosaic (detector array) sensors is the synthesis of algorithms to detect dim targets against earth backgrounds in the presence of several noise sources. Significant noise components are background drift, sensor jitter, background shot noise, detector crosstalk, system readout, and multiplexer (MUX) noises. In many applications the implementable signal processing algorithms are limited by the large number of detector channels required for adequate spatial sampling resolution and coverage. Consequently, filtering algorithms must be simple and must provide, under given constraints on memory and computing capacity, reliable detection at low input signal-to-noise ratios against severe and varying background conditions. The overall performance of a dim target detection system is limited by the amount of SNR enhancement which can be achieved by a filter applied to the raw focal plane data. Because of the large amount of data generated by a mosaic sensor, a primary goal of each detection algorithm block is to reduce the dimensionality of the problem such that the final step can be a simple threshold-type classification. To first order, sensor transfer characteristics are linear as shown in Fig. 2. Ideal and optimum filters can be synthesized directly from linear models of

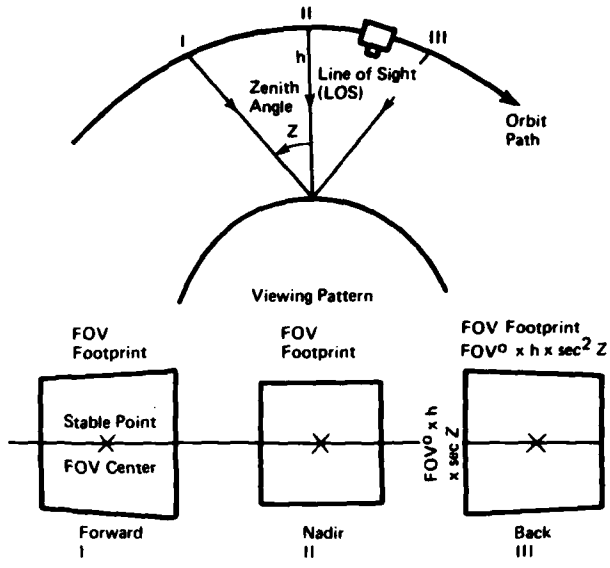

Fig. 1. Earth Surface Aim Point Viewing Geometry

the sensor and its inputs. In the context of this report, an "ideal" filter is one that is not constrained to be realizable while an "optimum" filter must be realizable within the constraints of a given filter configuration. This paper will include:

1. Discussion of the expected earth background drift velocities that a staring sensor in a low earth orbit (LEO) will encounter, and characterization of such drift in terms of orbital and earth viewing parameters.

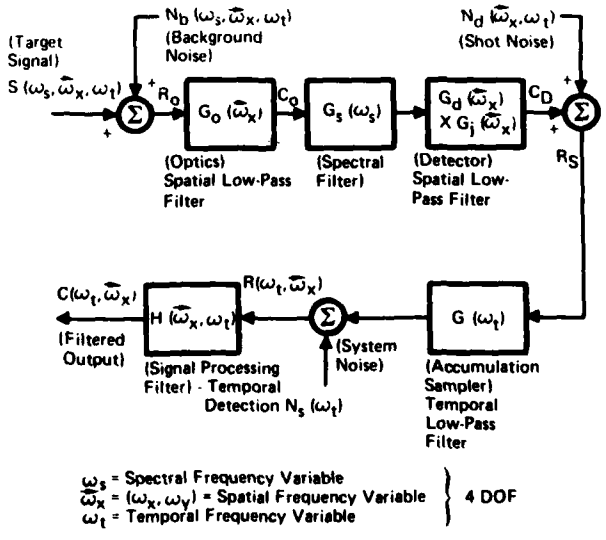

Fig. 2. A Functional Block Diagram of the Front End of a Typical Imaging Sensor System

2. Presentation of simple temporal filtering algorithms, and a comparative analysis of the effectiveness of various signal processing algorithms in rejecting background clutter noise.

3. The interrelationship between blur circle size and the consequent theoretical limit in achievable SNR.

The results summarized in this paper were obtained under a Rockwell IR&D effort and are explained in more detail in Reference 1. Some earlier results obtained under this same IR&D effort were reported in Reference 2 and also are included in this paper.

II. Characterization of Earth Background Drift

If we ignore the earth's rotation, the apparent angular motion of a ground point on the edge of the sensor FOV is given by[1]

$$\omega = \frac{\overline{V}_s}{r_1\, r_0} \times \Delta\overline{r}_{0c} \qquad (1)$$

where, referring to Fig. 3a,

$\overline{V}_s$ is the sensor linear velocity in the satellite orbit plane

$\overline{r}_1$ is the vector to the point of interest on the edge of FOV

$\overline{r}_0$ is the vector to the FOV stable point on the ground

$\overline{r}_{0c}$ is a vector equal in magnitude to Δr

A similar derivation is applicable to the study of apparent motion of other points on the edge of the sensor FOV. The net motion along the xyz axes with the x axis parallel to the satellite velocity in the orbital plane can be computed by resolving the $\overline{r}_1$ vector into three components (viz., $\overline{r}_{1x}$, $\overline{r}_{1y}$ and $\overline{r}_{1z}$,) and then taking the vector cross-product of each with the satellite velocity vector $\overline{V}_s$. Fig. 3b illustrates such a procedure. Depending on the position of the point of interest (target) in the sensor FOV, it can have simple linear motion or combined linear and rotational motion about the FOV center. For small FOV's, the magnitude of the motion of any point in the sensor FOV is linearly proportional to its distance from the FOV center, the stable point on the ground. Thus, results shown in this study for the perimeter of a square FOV can be extrapolated to larger FOV's or to circular FOV's.

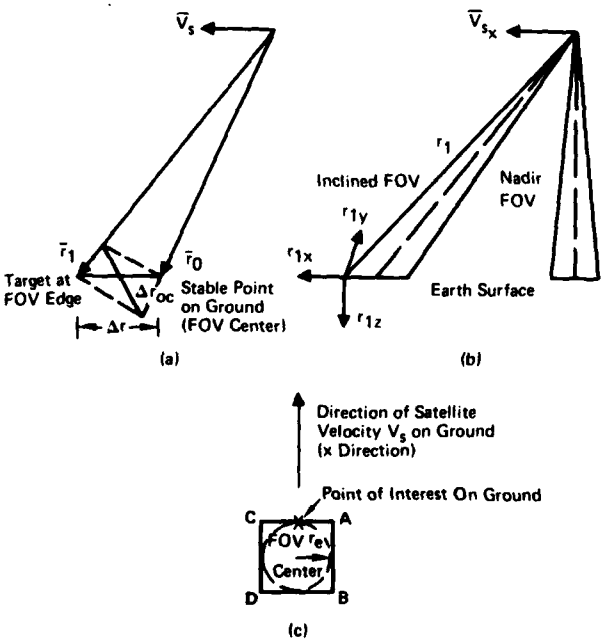

Fig. 3. Background Motion Calculation Geometry

System parameters used to study background motion dependence on sighting geometry are shown in Table 1. For the first part of the study to determine the dependence of drift parameters on satellite orbit altitude and zenith angle, three orbit altitudes–400 n.mi. (741.2 km), 1000 n.mi. (1853 km), and 3440 n.mi. (6374 km)–were picked and for each orbital altitude, four in-plane sighting geometries were chosen with satellite zenith angles of 30°, 45°, 60° and 80°.

Table 1. System Parameters to Study Background Motion Dependence on Sighting Geometry

Parameter	Characteristics
Circular satellite orbit	--
Orbit inclination	0° (equatorial)
Orbit altitude	254 km (137 n.mi.) - 6374 km (3440 n.mi.)
Satellite orbit period range	1.495 hr - 4.00 hr
Satellite zenith angle WRT local vertical of earth aimpoint	30-80°
Earth aimpoint/center of FOV	Latitude range = 0-19° Longitude range = 3.6-50.5°
Longitude at apogee	0°
Argument of perigee	0°
1/2 focal plane angle Forward FI Side S1	 0.75° 0.75° } square FOV
Sighting geometry	Along orbital plane forward of direction of motion; 60° to side in plane perpendicular to orbit plane

There are two more meaningful measures of angular drift other than the maximum angular drift, $|TO|_{max}$, the latter occurring at one or two of the four corners of a square or rectangular FOV. Using linear interpolation it is easy to derive the average drift (average of eight points) on the circumference of a circular FOV with radius r_e, $|\overline{TO}|_{r_e}$, circumscribed inside the square FOV as in Fig. 3c. Given the value of $|\overline{TO}|_{r_e}$, it is simple to derive[1] the value of the second important drift averaged over the area of a circular FOV of radius r_e to be

$$|\overline{TO}|_{FOV} = \frac{2}{3}\,|\overline{TO}|_{r_e} \qquad (2)$$

The values of maximum angular and linear background drift parameters have been plotted against various pertinent orbital parameters. Fig. 4 shows the magnitude of the maximum total angular drift $|TO|_{max}$ (arc-sec/sec) as a function of the satellite orbit altitude (Fig. 4a) and zenith angle (Fig. 4b). The maximum magnitude of the angular drift usually occurs at one or two of the four corners of a rectangular FOV and has, for constant zenith angles, a somewhat inverse relationship to orbit altitude. For constant satellite altitude, the magnitude of the maximum angular drift $|TO|_{max}$ increases markedly with higher satellite zenith angle, although the steepest increase takes place for satellite zenith angles greater than 60°, as shown in Fig. 4b.

Fig. 5 shows the various meaningful measures of angular drift and their dependence on satellite orbit altitude. Two sets of curves are plotted for the same satellite zenith angle (viz., 60°). One set refers to line of sight (LOS) 60° forward looking in the orbital plane and the other set refers to the LOS looking 60° to the side at right angles to the orbital plane. Typically, the angular drift rate looking sideways is significantly less than looking along the orbital plane for small (<1000 km) satellite orbit altitudes. Average drift magnitude on the circumference of a circular FOV is roughly 70% of the maximum drift value. It has been analytically shown that the angular drift averaged over the area of a circular FOV is 2/3 that of the angular drift on the circumference of the same FOV.

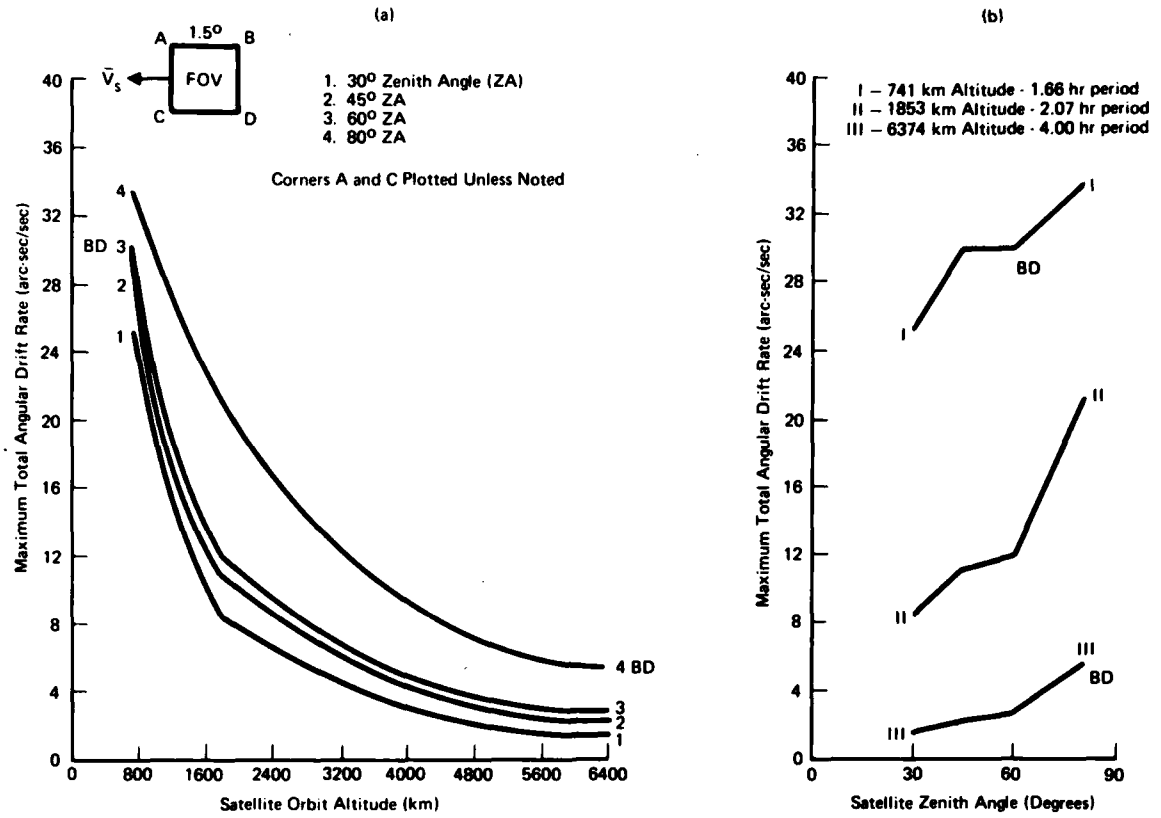

Fig. 4. Dependence of Maximum Total Angular Drift on Satellite Altitude and Zenith Angle

1-1 Maximum Total Angular Drift Rate on Perimeter of 1.5 x 1.5 Degrees Square FOV

2-2 Average of Total Drift Magnitude Over 8 Points on Circumference of 1.50° Circular FOV:

3-3 Average of Total Drift Magnitude Over 1.50° Circular FOV:

Upper X-X – 60° Forward Looking (Solid Curves)

Lower X-X – 60° Side Looking (Dashed Curves)

A and C Plotted Unless Noted

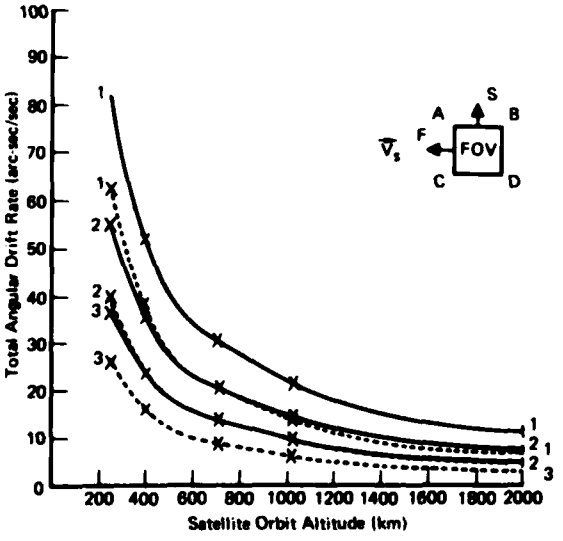

Fig. 5. Dependence of Apparent Background Angular Drift Rates on Satellite Altitude (Zenith Angle 60°)

The variation of the apparent background linear drift velocity orthogonal to LOS with orbital altitude is less than one might expect because angular drift has an inverse relationship with slant range for the same satellite zenith angle. This is illustrated by the two curves of Fig. 6, which show linear drift to be much less dependent on orbital altitude over the range shown. This is particularly true for the forward-viewing case, which is also the worst case.

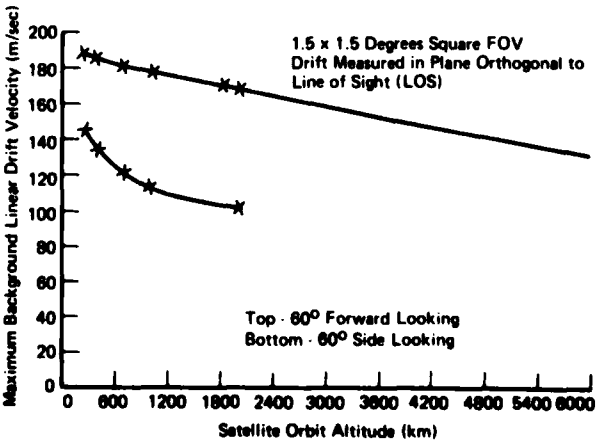

Fig. 6. Dependence of Apparent Background Linear Drift Velocity on Satellite Altitude

III. Performance of Various Digital Filters in Suppressing Background Clutter

One approach to handling background motion is to estimate this motion and then compensate the received image data so as to remove it. The algorithms required to perform high accuracy image motion compensation are not simple enough to be practically applicable to large array staring mosaic sensors. Another approach presented here, is to use SNR enhancement filters that exhibit sufficient performance in spite of excessive background motion. Given the target signal magnitude of Fig. 7 and sampled background clutter of Fig. 8, it is possible to use a high band pass filter to reject the low-frequency background clutter and retain the high-frequency components of signal magnitude, thus significantly improving the input SNR throughput. For detecting point source targets moving against structured background, we use primarily the classical detection (i.e., pre-whitened matched) filter. This filter can be written as $H_I(j\omega) = S(-j\omega)/|N(j\omega)|^2$ where $S(j\omega)$ is the signal and $N(j\omega)$ the additive noise. This filter optimizes the peak signal to rms noise ratio (SNR) and is typically the best when SNR gain is the overriding consideration. In Reference 2 it has been shown that, as a least-square estimator, the realizable filter $H_A(j\omega)$, as an approximation to the ideal filter $H_I(j\omega)$, is optimum with an acceptable delay α if the performance parameter given by

$$P = \int_{-\infty}^{+\infty} |R(j\omega)|^2 \left| H_I(j\omega) - e^{\alpha j\omega} H_A(j\omega) \right|^2 d\omega \qquad (3)$$

has been minimized, where $R(j\omega)$ is the Fourier transform of the total filter input. The examples of the optimum linear filter approximations presented in later sections were obtained by minimizing this performance parameter.

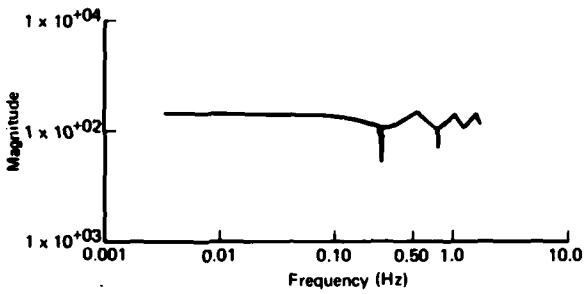

Fig. 7. Sampled Signal Magnitude Spectrum (1-Second Sampling Interval)

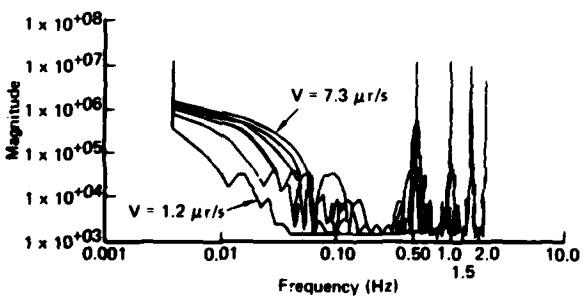

Fig. 8. Sampled Noise Magnitude Spectra (1-Second Sampling Interval)

Because of the nature of the multiplexed data stream out of a mosaic sensor, the required linear filters are sampled-data rather than continuous. Hence, account must be taken of fold-over or aliasing and the bandwidth limit specified by the sampling theorem.

In the simplest approach to temporal filtering, one matches the target detector cell dwell time to the detector integration time and the sampling period and then performs some order of temporal differencing. A slightly more complicated approach is to employ a temporal recursive filter and sample with a period less than or equal to the target cell dwell time. As will be shown later, this second approach offers greater system flexibility and performance at a slight increase in complexity.

To compare the performance of various filters as applied to the suppression of background clutter, a computer program was used to simulate a set of fixed (first through fourth) difference filters as well as to optimize a set of third-order recursive filters for six different drift rates. To show that the fixed difference filters are special cases of optimum filters of the same order, we start with a temporal filter with a third-order recursive structure as shown in Fig. 9. The filter is assumed to have a transfer function H(Z) expressed in the Z domain as,

$$H(Z) = \frac{Z+\alpha_0}{Z+\alpha_p} \times \frac{Z^2 + 2\,\xi_0\,\omega_{N0}\,Z + \omega_{N0}^2}{Z^2 + 2\,\xi_p\,\omega_{Np}\,Z + \omega_{Np}^2} \qquad (4)$$

$$= \frac{Z+K_2}{Z+K_1} \times \frac{Z^2 + K_4 Z + K_6}{Z^2 + K_3 Z + K_5}$$

By setting $\alpha_0 = K_2 = -1$, $\xi_0 = 0.5$, $K_4 = -2$ and $\omega_{NO}^2 = K_6 = 1$, and all other coefficients equal to zero, H(Z) of Fig. 9 becomes a third differencing filter $H(Z) = (Z-1)^3/Z^3$ which is a concatenation of three first difference filters [vis., $(Z-1)/Z$].

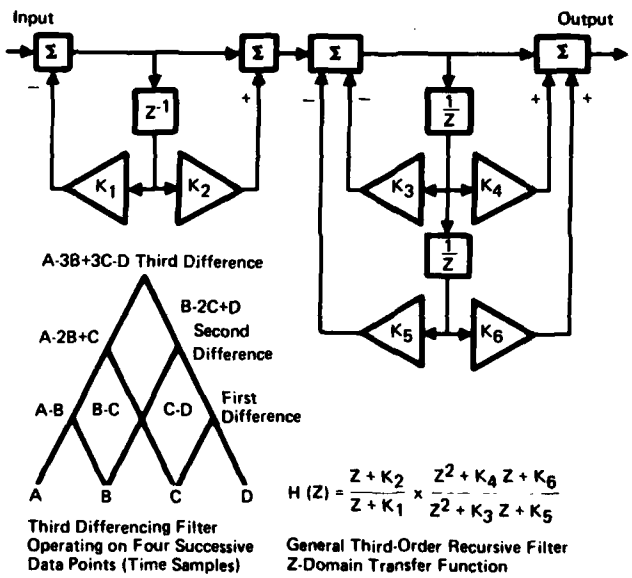

$K_1 = \alpha_p = 0$
$K_3 = 2\,\xi_p\omega_{Np} = 0;\ K_5 = \omega_{Np}^2 = 0$
$K_2 = \alpha_0 = -1;\ K_4 = 2\,\xi_0\omega_{NO} = -2;\ K_6 = \omega_{NO}^2 = 1$

} Third Difference Filter $\frac{(Z-1)^3}{Z^3}$

$$H(Z) = \left(\frac{Z+\alpha_0}{Z+\alpha_p}\right)\left(\frac{Z^2 + 2\,\xi_0\,\omega_{NO}\,Z + \omega_{NO}^2}{Z^2 + 2\,\xi_p\,\omega_{Np}\,Z + \omega_{Np}^2}\right)$$ Alternate Expression for Third-Order Recursive Filter

Fig. 9. General Third-Order Recursive Temporal Filters

Letting all of the filter coefficients, α_0, ξ_0, ω_{NO}, α_p, ξ_p and ω_{Np} of Equation 4 vary, a set of six optimum third-order recursive filters was synthesized to best match the ideal filter transfer functions according to the criterion set by Equation 3. The coefficients of these optimum third-order recursive filters which depend both on background drift rate and sampling interval are shown in Tables 2 and 3.

Table 2. Coefficients for Optimum Recursive Filters-Sampling at Intervals of 1/2 the Target Cell Dwell Time

V_b (μr/s)	α_0	ξ_0	ω_{N0}	α_p	ξ_p	ω_{Np}
7.3	-1.086	-1.040	0.756	0.005	0.091	0.823
6.1	-1.716	-1.163	1.758	0.279	0.146	0.842
4.8	-1.001	6.612	-2.623	0.253	0.077	0.824
3.7	-1.002	2.323	-1.379	-0.193	-0.367	0.759
2.4	-0.986	-1.000	0.994	-0.789	0.678	-0.774
1.2	0.205	-1.000	1.015	-0.370	0.450	-0.606

Table 3 Coefficients for Optimum Recursive Filters Sampling at the Target Cell Dwell Time

V_b (μr/s)	α_0	ξ_0	ω_{N0}	α_p	ξ_p	ω_{Np}
7.3	-0.996	-1.284	0.287	0.802	0.768	0.876
6.1	-1.000	-0.854	1.127	0.680	0.656	0.714
4.8	-0.999	-0.942	0.884	0.414	0.464	0.648
3.7	-1.003	-1.004	1.23	0.462	0.156	0.704
2.4	-0.711	-1.000	0.963	0.186	0.448	-0.706
1.2	-1.027	-1.002	1.055	0.436	0.920	-0.411

Some of the limiting assumptions used for this study:

- A stochastic quasi-linear model of the detector process is adequate.
- Noise and background are additive, uncorrelated, and generated by a Gaussian random process with a given power spectral density (PSD).
- Target is additive.
- Sensor and filter responses are linear.
- Background and target velocities are constant with a fixed detector crossing geometry.

System parameters used in our study are shown in Table 4.

Fig. 7 shows the sampled signal magnitude (sampling interval of 1 sec) and noise magnitude spectra up to a frequency range of 2 Hz and clearly shows the effect of sampling frequency on resulting spectra. Fig. 8 is especially useful as it also illustrates the effect of background motion on background clutter spectra and hence, the total noise spectra. Fig. 8 is indeed a super-position of six cases for six background drift rates (7.3μ r/s to 1.2 μ r/s in equal decrement interval).

Table 4. Assumed System Parameters for Filter Design to Suppress Background Motion Effects

Parameter	Characteristics
Sensor altitude	3,600 km
Target	Point source Velocity aligned with footprint side; 200 m/sec
Background	1/f PSD; Gaussian PDF; angular drift velocity V_B: 1.2 μR/S to 7.3 μR/S; rotational drift about FOV center neglected
Optics	Circular clear aperture diffraction-limited blur circle calculation based on $\lambda = 8.7$ μm
Transmissivity	Aperture-to-focal plane 50%; spectral filter 25%
Detectors	Square area > blur circle; uniform responsivity
Shot noise	RMS shot/RMS background = 3.69×10^{-3} White Gaussian
Other noise	No jitter, system noise, crosstalk, MUX noise
Sample time/integration time	1-sec = 1/2 target cell dwell time: first set of test cases 2-sec = target cell dwell time: second set of test cases
Sampling and integration time	Varied jointly with respect to the cell dwell time
FOV	Square footprint with 400 m side
Input peak signal to σ of total noise	0.238 at $V_b = 1.2$ μR/S 0.052 at $V_b = 7.3$ μR/S

Fig. 10 is the impulse response of a first difference filter. The time of the impulse has been arbitrarily set at 50 sec. Note that due to the property of first difference, we obtain two samples from an unblurred point target, of equal but opposite magnitude and set apart by the sampling interval. The impulse responses are invariant with respect to the background drift rates but do depend on the sampling interval. Note that for a fixed-difference filter, the number of "positive" and "negative" samples associated with the magnitude response is one higher than the order of the filter (2 for a first difference filter in Fig. 10, for example). All of the preceding statements can be understood by examining the value of the coefficients in the "tree diagram" of Fig. 9.

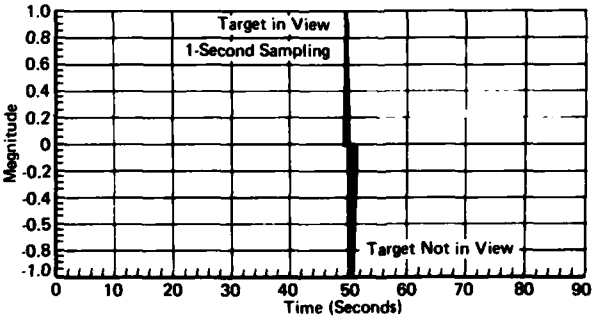

Fig. 10. First Difference Filter Impulse Response (Same for all Drift Rates) 1-Second Sampling

Fig. 11 shows the impulse response for the optimum third-order recursive filter which was derived from the corresponding ideal filter. It should be obvious that transversal filter approximations to these characteristics would require many more than just three delay stages. The impulse responses for the third-order optimum recursive filters vary with both the sampling interval and the background drift rate since the filter assumes different coefficient values (given in Tables 2 and 3), depending on the sampling interval and the background drift rates. Notice also that while the ideal (non-realizable) filter is non-causal, the optimum recursive filter being realizable has a causal impulse response. Also, the damping of the impulse response depends on the background motion. For the optimum recursive filters a sharper frequency domain cutoff and, hence, smaller damping coefficient is required for high background drift rate.

Fig. 12 and 13 show the peak normalized magnitude responses of the various fixed-difference, ideal, and third-order optimum recursive filters to a frequency range of 1 Hz. These figures illustrate the advantages of optimum recursive over fixed-difference

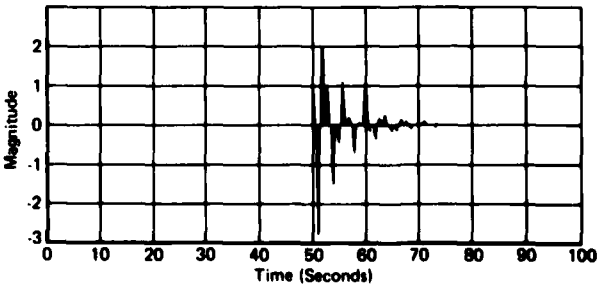

Fig. 11. Optimum Third-Order Recursive Filter Impulse Response ($V_b = 7.3$ μr/s) 1-Second Sampling

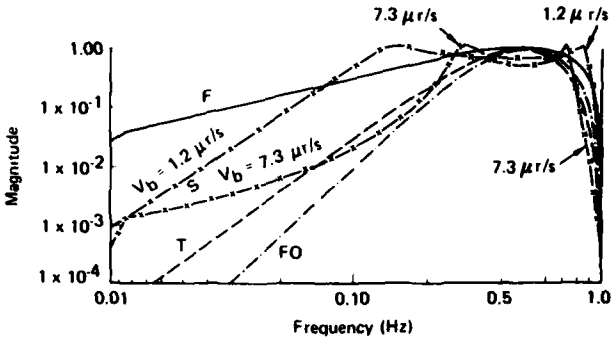

Solid Curve (F):	First Difference Filter
Long Dashed Curve (S):	Second Difference Filter
Dashed Curve (T):	Third Difference Filter
Dash-Dot Curve (FO):	Fourth Difference Filter
Dash-X Curves With V_b Values:	Third-order Optimum Recursive Filters

Fig. 12. Magnitude Responses of Various Fixed Difference and Third-Order Recursive Filters (1-Second Sampling for Optimum Recursive Filters)

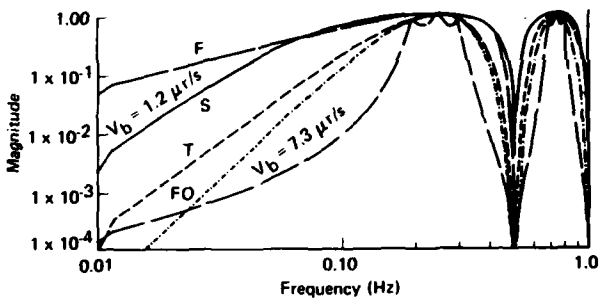

Solid Curve (F):	First Difference Filter
Long Dashed Curve (S):	Second Difference Filter
Short Dashed Curve (T):	Third Difference Filter
Shorter Dashed-Dotted Curve (FO):	Fourth Difference Filter
Curves With V_b Values:	Third-Order Optimum Recursive Filters
Solid Curve:	Optimized for V_b = 1.2 μr/s
Long Dashed Curve:	Optimized for V_b = 7.3 μr/s

Fig. 13. Magnitude Responses of Third-Order Optimum Recursive and Fixed Difference Filters (2-Second Sampling for Optimum Recursive Filters)

filters of first through fourth orders. For a sampling time interval of 1 sec, (over sampled case) Fig. 12 shows that for high background drift rate (7.3 μrad/sec), the third-order recursive filter has a greater background clutter rejection than the first- and second-difference filters but has less background rejection capability than the fourth-difference filter. For lower background drift rates (e.g., 1.2 μrad/sec) in the oversampled case (Fig. 12), the third-order recursive filter, optimized for V_b = 1.2 μrad/sec, offers a broader passband than the second, third-, and fourth-difference filters. This feature allows for integration against the white shot noise which determines the SNR over the background drift effects for low background motion. When sampling interval coincides with target cell dwell time as in Fig. 13, the advantage of recursive filters over fixed-difference filters is again observed. The magnitude response curves of the two third-order recursive filters for the extreme values of the background drift rates span the magnitude response curves for the second-, third-, and fourth-difference filters. This implies that by adaptive adjustment of its coefficient values in response to the existing background drift rate, the optimum recursive filter can indeed perform superior to the second-, third-, and fourth-difference filters in rejecting background clutter.

In Fig. 14 and 15 are plotted the maximum peak signal to rms noise versus the background drift rates of interest as output by the various fixed-difference, ideal, and optimum recursive filters.

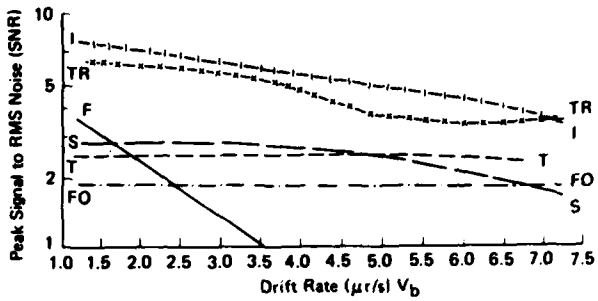

Solid Curve (F):	First Difference Filter
Long Dashed Curve (S):	Second Difference Filter
Dashed Curve (T):	Third Difference Filter
Dash-Dot Curve (FO):	Fourth Difference Filter
Dash-X Curve (TR):	Third-Order Optimum Recursive Filters
Dash-I Curve (I):	Ideal Filters

Fig. 14. Effectiveness of Various Filters in Suppressing Background Motion Effects (1-Second Sampling Time)

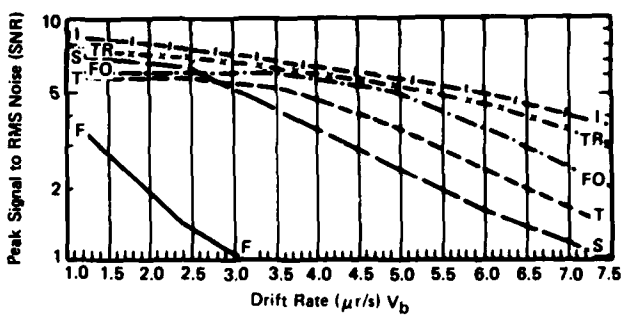

Solid Curve (F):	First Difference Filter
Long Dashed Curve (S):	Second-Order (Fixed) Difference Filter
Dashed Curve (T):	Third-Order (Fixed) Difference Filter
Dash-Dot Curve (FO):	Fourth Difference Filter
Short Dashed -X Curve (TR):	Third-Order Optimum Recursive Filters
Dash-I Curve (I):	Ideal Filters

Fig. 15. Effectiveness of Various Filters in Suppressing Background Motion Effects (2-Second Sampling Time)

Figs. 14 and 15 assume that the beginning of the sampling interval is synchronized with the passage of the target across the detector window, such that during the sampling interval the detector collects the maximum possible amount of the target energy.

Fig. 14 and 15 show the effectiveness of the optimum third-order recursive filters (curves labeled TR at two ends) in suppressing background motion effects on peak SNR, respectively. For a sampling interval of 1 sec, Fig. 14 shows that for lower drift rates (< 4.9 μ rad/sec), the third-order recursive filter optimized for the same drift rates have more than a factor of 2 SNR advantage over equivalent third-difference filter; at higher drift rates the SNR improvement is less dramatic as the effect of non-optimum sampling/integration interval affects the performance of the recursive filters more than the performance of third- and fourth-difference filters. Among the first- through the fourth-order fixed-difference filters, for all ranges of drift rates and sampling intervals, the performance of the first-difference filter is decidedly the worst. Sampling time interval has a significant influence on the relative performance of various orders of fixed-difference filters. When the sampling frequency is 1 Hz (Fig. 14), for lower drift rates (< 5.0 μ rad/sec), the second-difference filter is superior to the third-difference filter, which is in turn superior to the fourth-difference filter. For the range of drift rates considered for this study (maximum 7.5 μ rad/sec), there is no advantage in using fourth-difference filter over third-difference filter for the oversampled case, but as shown in Fig. 15 and Table 5, for higher drift rates, such may not be the case. Again, for the range of low

Table 5. Summary of Results Peak Output SNR Gain Calculations

Case Number	Target Velocity V_t (m/s)	Cell Dwell Time (sec)	Sampling/ Integration Time (sec)	BG Drift Rate V_b (μr/s)	Peak SNR Fixed-Difference Filters				Peak SNR Ideal Filter	Peak SNR Optimum Recursive	
					First	Second	Third	Fourth		Third-Order	High V_b
					Case 1-1	Case 2-1	Case 3-1	Case 4-1	Case 5-1	Case 6-1	Case 7-1
A	200	2	1	7.3	0.50	1.68	2.27	1.862	3.48	3.49	3.49
B	200	2	1	6.1	0.66	2.14	2.44	1.902	4.37	3.36	3.80
C	200	2	1	4.9	0.91	2.55	2.510	1.912	5.03	3.77	3.88
D	200	2	1	3.6	1.33	2.77	2.528	1.914	5.94	5.15	3.906
E	200	2	1	2.4	2.25	2.86	2.531	1.915	6.89	5.92	3.910
F	200	2	1	1.2	3.71	2.87	2.531	1.915	7.79	6.25	3.911
					Case 1-2	Case 2-2	Case 3-2	Case 4-2	Case 5-2	Case 6-2	Case 7-2
A	200	2	2	7.3	0.27	1.07	1.50	2.14	3.77	3.16	3.17
B	200	2	2	6.1	0.36	1.58	2.33	3.39	4.96	4.33	3.97
C	200	2	2	4.9	0.50	2.51	3.70	5.04	5.75	5.34	4.488
D	200	2	2	3.6	0.74	4.13	5.13	5.98	6.67	6.15	4.514
E	200	2	2	2.4	1.37	6.38	5.72	6.16	7.58	6.98	4.519
F	200	2	2	1.2	3.44	7.13	5.76	6.17	8.42	7.51	4.521

background drift considered. for the oversampled case, the peak SNR performances of the third- and fourth-difference filters appear almost unchanged (Fig. 14), as the shot noise is unaffected by the drift rate, and most of the low V_b clutter has been eliminated by high difference filters. The cross-over of the third-order recursive filter maximum SNR with that of the ideal filter in Fig. 14 is caused by computational approximation in the computer simulation. From a physical standpoint the performance of all filters, including the optimum recursive, suffers with increasing background drift rates.

When the negative effects of oversampling are eliminated by using a sampling/integration interval equal to the cell dwell time, the superiority of the optimum recursive filter over the various orders of fixed-difference filters is more clearly demonstrated. This is because a recursive filter can compensate for improper target integration while a fixed-difference filter can not. While a second-difference filter may yield higher peak SNR's (in Fig. 15) than third- and fourth-difference filters for low (<2.5 μ rad/sec) drift rates, for higher (>2.5 μ rad/sec) drift rates, the higher the difference filter order, the better is the SNR performance. This is because lower order difference filters degrade the target less for low background drift rates. For higher drift rates (>7.0 μ rad/sec), the third-order recursive filters have almost a factor of 2 SNR over the third-difference filter. At lower drift rates, the improvement is less noticeable because shot noise dominates the total noise input. Note that the optimum recursive filter SNR performance is very close (within 10%) to that of the theoretically "ideal" filter for drift rates shown in Fig. 15. In Fig. 15, the first-difference filter has peak SNR's of less than 1 for drift rates higher than 3.1 μ rad/sec. It is not surprising that recent systems have not used first-difference filtering.

Since it may not be practical to adjust the filter coefficients adaptively for each drift rate for an optimum recursive filter, it is of interest to study the behavior of a recursive filter optimized for a particular drift rate (usually the highest expected drift rate) for other drift rate conditions. Such behavior is highlighted in Table 5 for a third-order recursive filter with constant filter coefficients optimized for a single drift rate of 7.3 μ rad/sec.

Comparing the last two columns of Table 5, we see that much of the filter performance is sacrificed at lower drift rates. However, the latter filter still gives higher peak SNR over the range of drift rates than the first- through the fourth-difference filters. When the effect of non-optimum (1-sec) sampling/integration time is eliminated from the problem conditions, we again find by comparing the last two columns of Table 5 that for lower drift rates (<3.5 μ rad/sec), the filter optimized for 7.3 μ rad/sec has a worse SNR than the fixed-difference filters except the first-order. However, as the drift rates approach the drift rate for which the filter was optimized, it performs better than any of the fixed-difference filters.

The results presented here show that: (1) the use of optimized recursive filters instead of fixed-differencing filters can result in significant improvements in SNR performance especially at higher (>5.0 μ rad/sec) drift rates; (2) in addition, by oversampling in time, dropouts due to phase mismatch between the target and sample time can be lessened; (3) for the first-, second-, and third-difference filters, SNR performance is slightly improved by oversampling (sampling interval 1/2 cell dwell time) at the highest drift rates (6.0 and 7.3 μ rad/sec) but significant SNR degradation results at the lower drift rates; (4) overall performance is degraded by not using an optimum target signal integration time and sampling interval, but that a recursive filter can be adjusted to compensate to a large extent (filter coefficients can be set in a third-order recursive filter so that both differencing at low frequencies to attenuate structured background and integration at high frequency to attenuate random system and detector shot noise can be provided); and (5) of the six different realizable filters considered in the study, the best SNR performance was achieved by using a third-order optimum recursive digital filter and oversampling for high background drift rates and sampling at the target cell dwell time for lower drift rates.

IV. Spatial Filtering Considerations

Another electro-optical system parameter that we may consider varying so as to improve the SNR performance is the optical blur circle size. To gain insight into the performance consequences associated with this parameter, we have posed and investigated the following problem:

> For the detection of moving targets immersed in a drifting structured background with a staring mosaic type sensor, derive an ideal cascaded pair of linear spatial and temporal filters.

For this problem we shall assume the system model given in Fig. 16. In addition, we shall assume the following:

1. The total input noise spectrum can be written as

$$N(\vec{\omega}_x,\omega_t) = N_b(\vec{\omega}_x) + N_t(\omega_t) + N_s(\omega_t)$$
$$= N_b(\vec{\omega}_x) + N_d(\omega_t)$$

where $N(\vec{\omega}_x,\omega_t)$ is the spectrum of the total input noise, $N_b(\vec{\omega}_x)$ is the spectrum of the background spatial structure, $N_t(\omega_t)$ is the spectrum of the background temporal fluctuation, and $N_s(\omega_t)$ is the spectrum of temporal random noise that is generated in the detector, and $N_d(\omega_t)$ is the total temporal noise.

2. The phase content of spectra can be ignored except for the computation of cross spectral densities.

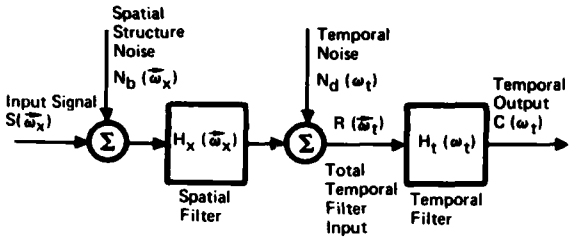

Fig. 16. Model of the Cascade Spatial-Temporal Filter

3. The background is drifting with velocity $\vec{V}_b$ and the target is drifting with velocity $\vec{V}_t$ such that for the background, $N_t = \vec{V}_b \cdot \vec{\omega}_x$; and for the target or signal, $\omega_t = \vec{V}_t \cdot \vec{\omega}_x$

4. There is zero correlation between the inputs $S(\vec{\omega}_x)$, $N_b(\vec{\omega}_x)$, and $N_d(\omega_t)$.

The ideal temporal filter, which will maximize at its output the ratio of the maximum of the signal to the rms of the noise, or, in other words, the SNR, can be written as[1]

$$H_t(\omega) = \frac{S(\vec{V}_t \cdot \vec{\omega}_x)\, H_x(\vec{V}_t \cdot \vec{\omega}_x)}{|N_b(\vec{V}_b \cdot \vec{\omega}_x)\, H_x(\vec{V}_b \cdot \vec{\omega}_x)|^2 + |N_d(\omega_t)|^2} \quad (6)$$

Such a filter has the property that the greater the integrated output spectrum $\int_{-\infty}^{\infty} C(\omega_t)\, d\omega_t$, the greater will be the output SNR. We can thus define an optimization parameter P which we will want to minimize as

$$P = \int_{-\infty}^{\infty} \frac{1}{C(\omega_t)}\, d\omega_t \quad (7)$$

Because the cross-spectra terms vanish, Equation 7 can be reduced to[1]

$$P = \int_{-\infty}^{\infty} \left(\frac{|N_b(\vec{V}_b \cdot \vec{\omega}_x)|^2}{|S(\vec{V}_t \cdot \vec{\omega}_x)|^2} \frac{|H_x(\vec{V}_b \cdot \vec{\omega}_x)|^2}{|H_x(\vec{V}_t \cdot \vec{\omega}_x)|^2} + \frac{|N_d(\omega_t)|^2}{|S(\vec{V}_t \cdot \vec{\omega}_x)|^2} \frac{1}{|H_x(\vec{V}_t \cdot \vec{\omega}_x)|^2} \right) d\omega_t \quad (8)$$

From this equation we observe that, compared to no spatial filtering ($H_x(\vec{\omega}_x) = 1$), a spatial filter will improve the signal to background structure by a factor of

$$\frac{|H_x(\vec{V}_t \cdot \vec{\omega}_x)|^2}{|H_x(\vec{V}_b \cdot \vec{\omega}_x)|^2}$$

and the signal to purely temporal noise by a factor of $|H_x(\vec{V}_t \cdot \vec{\omega}_x)|^2$ at each frequency.

Let $G_x(\omega_t)$ be the gain in signal to background that will be achieved by a spatial filter

$$G_x(\omega_t) = \frac{|H_x(\vec{V}_t \cdot \vec{\omega}_x)|^2}{|H_x(\vec{V}_b \cdot \vec{\omega}_x)|^2} \quad (9)$$

To gain insight into the behavior of $G_x(\omega_t)$ let us consider the following example. Let $N_d(\omega_t) = 0$ and let $H_x(\vec{\omega}_x)$ be the lowpass filter of Fig. 17. Now let $H_x(\vec{\omega}_x)$ be the highpass filter of Fig. 18.

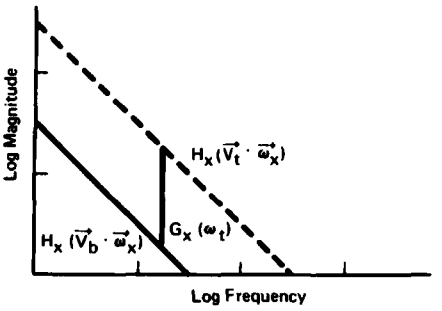

Fig. 17. Illustration of the Signal-to-Background Enhancement Obtainable From a Low-Pass Spatial Filter

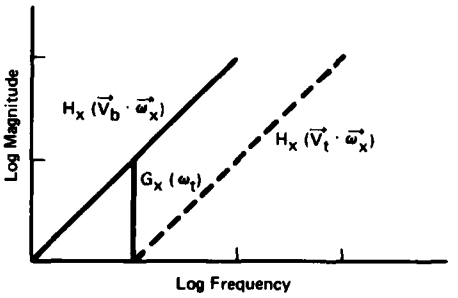

Fig. 18. $H_x(\vec{\omega}_x)$ as a High-Pass Filter

It appears that the spatial filter will, as a lowpass filter, yield a gain in signal to background as a function of frequency for a target faster than the background drift. A highpass spatial filter will tend to degrade this performance.

Furthermore, as we decrease the resolution of a typical optical system we should observe the following:

1. We can achieve a performance gain against background as expressed in Equation 9. We also observe as shown in Fig. 19 that the greatest gain will occur at the higher frequencies.

2. We lose in performance against temporal noise by a factor $G_t(\omega_t)$.

$$G_t(\omega_t) = H_x(\vec{V}_t \cdot \vec{\omega}_x) \quad (10)$$

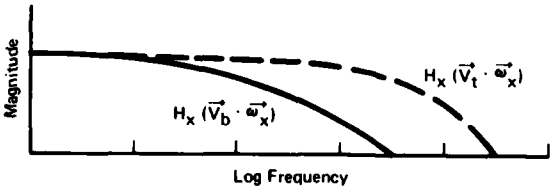

Fig. 19. A Typical Optical Low-Pass Filter

From our work we have observed that as we increase the blur circle size we always lose SNR at the lower drift rates but we gain a potential for improved SNR at higher drift rates. Another observation is that as the blur circle is increased the breakeven point for SNR versus blur circle size migrates to higher drift rates so that for each drift rate there will be some single optimum blur circle size depending on the drift rate. Another observation is that as the blur circle is increased, temporal filters with sharper band edge cutoffs are required to achieve ideal performance.

To achieve such sharper band edge cutoff, as shown in the previous section, one must use more generalized recursive filter structures instead of just simple structures associated with differencing filters.

V. Summary/Conclusions

Summarizing, the most critical problem in space-based staring-mosaic-sensor surveillance systems is that ideal staring operation cannot be achieved with non-synchronous observer orbits looking at earth backgrounds: background appears to drift everywhere in the FOV except the stabilized center. The objectives of this study have been threefold:

1. To characterize earth background drift versus orbit.
2. Compare effectiveness of signal processing algorithms in rejecting the background clutter noise.
3. Use of spatial filtering effects in suppressing background clutter.

The following were the most significant results of our study:

1. For fixed angular FOV:
   a. Background drift in angular measure (arc-sec/sec) decreases markedly with observer altitude (Fig. 4a).
   b. Angular drift rate varies considerably with viewing geometry. A factor of 2.5 to 1.5 increase results (depending on orbit altitude) from increasing LOS zenith angle (angle between LOS and local vertical at LOS intersection with the ground) from 30 to 80° (Fig. 4b). Since range also increases with increasing zenith angle, apparent linear drift on the ground increases even more.
   c. Background drift in linear measure (meters/sec) changes little with altitude (Fig. 6).
2. Assuming drift varies linearly with distance from FOV center, average angular drift in a circular FOV is two-thirds of the worst-case drift at the edge of the FOV. Average drift at the periphery of a circular FOV is approximately 70% of the maximum drift at one or more corners of the circumscribed square FOV. For fixed coverage on the ground, requiring smaller FOV for higher observer altitude, linear drift (m/sec) and hence, background clutter noise decreases with altitude; this implies higher orbits should be favored for aircraft detection.
3. One can obtain significantly better SNR performance from an optimized recursive filter than from an equivalent fixed-differencing filter, especially at higher drift rates. For equal performance, FOV area for a third-order recursive filter equals four times the FOV area for a third-difference filter; the latter implying step-stare update rate of four times as much as for a recursive filter (Fig. 14 and 15). Higher order filters are quite effective in improving clutter noise rejection. In one sample case, for higher drift rates, a third-order recursive filter permitted only one-half of the clutter leakage of a third-differencing filter which in turn permits about one-half of the clutter leakage of a second-difference filter.
4. While the performance of fixed-differencing filters is severely degraded (if the sample rate is higher than the target cell dwell time), recursive filters can be adjusted to compensate for the non-optimum detector integration time. In addition, by oversampling in time, dropouts due to phase mismatch between the target and the sample time can be minimized. Parameters can be set in a third-order recursive filter so that both differencing at low frequencies to attenuate structured background and integration at high frequency to attenuate random system and detector shot noise can be provided. To summarize, we have shown that superior performance can be achieved using an optimum recursive digital filter (and oversampling in time for high background drift rates and sampling at target cell dwell time for low drift rates) than from a fixed differencing filter operated at one sample per target cell dwell time.
5. A recursive filter that is optimum for a given background drift rate will exhibit somewhat higher SNR's than fixed difference filters when the background drift rate is actually lower than assumed (Table 5).
6. Peak signal to rms background clutter can be improved by increasing the optical blur circle size and using a temporal filter with a sharper band edge cutoff. However, as the blur circle is increased, peak signal to rms shot and system noise will be decreased.

Acknowledgements

The authors are grateful to M. Sentovitch of Rockwell International for the technical help in modeling the background motion. They also thank Dr. R. Ennulat, Director of Rockwell's Electro-Optical Laboratory, for a careful review of the manuscript.

References

1. Mukhopadhyay, A.K., and W.H. Haas, Background Motion Effects on Staring Sensors. Final Report of IR&D Project No. 29630, Rockwell International, SSD 79-0181 (Oct. 1979).
2. W.H. Haas et al, "Performance of Mosaic Sensor Dim Target Detection Algorithms," Proc. SPIE, Vol. 178 (April 1979), pp. 25-32.